Camera Calibration Using Fiducial Markers: A Novel Tool for Automated PIV Systems

A. Brunn[1*], O. Tedjasukmana[1], F. Michaux[1], C. Willert[2] & S. Kallweit[3]

[1] iLA 5150 GmbH, Aachen, Germany

[2] DLR Institute of Propulsion Technology, German Aerospace Center, Cologne, Germany

[3] University of Applied Sciences in Aachen, Germany

[*] corresponding.author@ispiv.com

Abstract

Large-scale PIV system setup requires precise manipulation of every component, which is made possible using industrial robots. The precise positioning of the individual PIV components in accordance with the measurement requirements is made possible by the cameras' known internal calibration matrix, the real pose of the industrial robots, and the computed transformation from the fiducial markers to camera coordinates.

Furthermore, the degree of automation can be maximized since the entire calibration process for creating the external camera matrix and the mapping functions, such as de-warping the stereo images, can be automatically determined without additional user intervention. Particularly for measurement tasks with strict time constraints, the increased level of automation broadens the range of applications for PIV systems.

1 Introduction

Fiducial markers are commonly employed in numerous robotic and automated applications, primarily for perception and localization tasks. Various families of markers exist (Garrido-Jurado et al., 2014; Zakiev et al., 2020), with properties that can be customized for specific applications, including visibility, size, information content, detection speed, and detection stability (Krogius et al., 2019). All optical markers utilize a monocular camera image, which delivers the complete 6D pose of the represented marker.

The transformation between the camera and marker coordinates is thus established. Using the established internal camera matrix, readily obtainable from the specifications of the utilized camera and a high-quality lens, the 6D pose of a specific marker, such as a *AprilTag* (Olson, 2011), can be ascertained for subsequent calibration or positioning procedures.

The increased detection uncertainty of a single marker's pose and potential occlusions necessitate the use of a bundle of markers. A checkerboard featuring *AprilTag* or *ArUcoTag* markers facilitates the 6D pose estimation of the entire calibration grid in camera coordinates, as illustrated in Fig. 1.

The established 6D pose of the robots in world coordinates is utilized to compute the transformations from robot coordinates to target coordinates. This process facilitates the control of individual camera-robot positions and the robot for the light sheet optics, thereby enabling an optimal configuration for the measurement task. A typical approach for stereoscopic PIV is shown in Fig. 2. Single level targets are sufficient instead of using multi-level calibration targets.

2 Procedure

The automatic calibration operation begins with positioning the calibration grid with the *ArUcoTag* bundle at the measurement location. This approach has been used by (Akamine et al., 2023) for the calibration of three-dimensional background-oriented schlieren (3D-BOS) involving 12 cameras. The calibration grid comprises a combination of ArUco (Garrido-Jurado et al., 2014) and standard checkerboard markers, referred to as *ChArUco* grids (Fig. 1). An initial estimation of the camera pose from the calibration grid image is ascertained and utilized to adjust the camera-robot accordingly. The marker
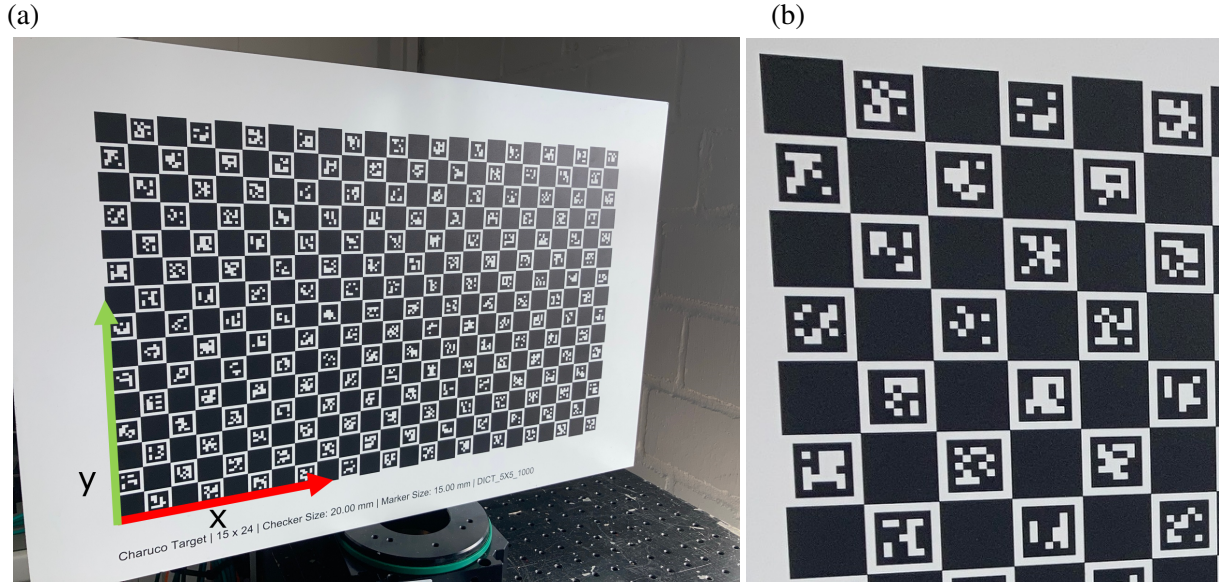
Figure 1: Calibration checkerboard (a) (*ChArUco*) with *ArUcoTag* bundle. (b) detail showing individual *ArUco* tags of type DICT_5x5_1000 each with 5×5 bit encoding.
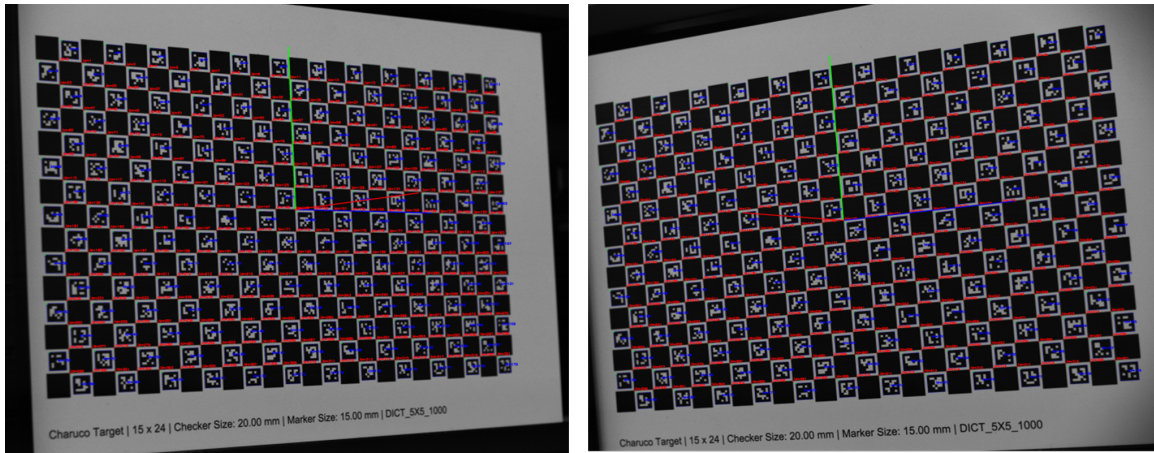

Figure 2: Calibration target with ChArUco-design with detected marker and corner ID's for stereoscopic camera views (left & right).

detection algorithm offers a transformation of the marker bundle coordinate frame depicted in (Fig. 1) to the camera coordinate system.

Utilizing the established static transformation from the robot's Tool Center Point (TCP) to the camera frame, the camera may now be translated and rotated to the specified point within the robot's coordinate system. The camera and light sheet angles can be automatically optimized. When the camera array—specifically two for a conventional stereoscopic method—is oriented towards the target, the predetermined quantity and dimensions of the calibration square points, stored within the selected tag family, are back-projected onto the calibration grid to compute the mapping function. The artificial markers in the calibration phase are positioned sufficiently near the checkerboard corners, allowing for precise determination of these corners' locations thereafter by a gradient-based sub-pixel approach (Fig 4).

The operation of the light sheet robot is conducted in accordance with the specified process. The disparity map is utilized to compute the translation and orientation of the light sheet relative to the calibration grid, thereby aligning it more precisely with the calibration target. This information is applicable in a closed-loop control system.

The suggested method requires just a modified calibration apparatus, which supplies the essential optical markers to facilitate the transformation between coordinate frames. Markers may be printed on existing calibration grids or utilized on newly redesigned calibration grids. Active lighting is unnecessary; ambient lighting conditions adequately suffice for capturing photos of the target for the specified
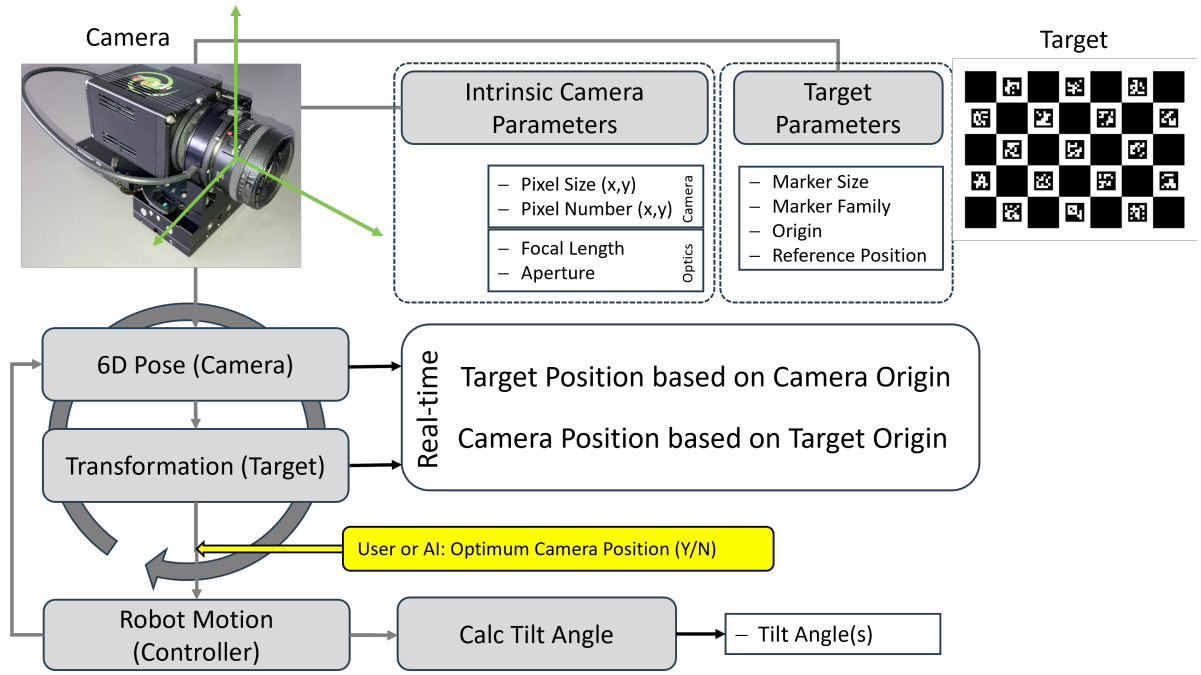
Figure 3: Scheme of a typical calibration process using a ChAruCo target and an imaging system (camera with lens) with known intrinsic parameters

calibration method. Furthermore, the markers can encode information within the calibration grid to activate specific pre-programmed functions, facilitating a fully automated setup and calibration process utilizing industrial robots. In scenarios lacking robots for camera and laser positioning, the method can nevertheless be employed to accurately align the PIV setup manually or via a motorized traversing unit, utilizing real-time camera pose estimate from the marker recognition algorithm.

It is sufficient for only portions of the entire ChAruCo target to be visible within the camera frame to ascertain the target's attitude, which is a significant benefit of the proposed method. The distinct ArUco markers on the calibration grid facilitate the creation of a correspondence list between real-world points and pixel points for the subsequent PIV mapping function. The actual world coordinates of the checkerboard corners are back-projected to pixel coordinates using the established transformation of the 6D pose in camera coordinates.

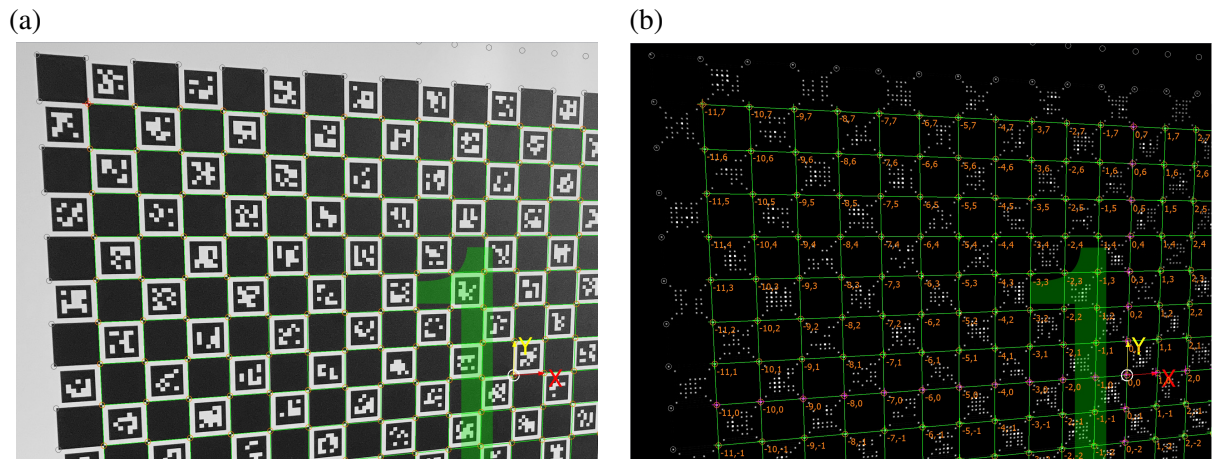(a)   (b)

Figure 4: Automated grid registration using sub-pixel accurate corner detection. (a) original image with overlaid grid, (b) image after applying corner detection and grid reconstruction.

3 Experimental Setup

To ascertain the measurement deviation in accordance with DIN 1319 (DIN, 1995), each measurement value comprises a systematic known deviation and an unknown (random) variation. The random variation can be quantified by statistical methods, commonly referred to as 'repeatability' in data sheets. The measurement uncertainty is determined through a statistical analysis of the results, utilizing the standard deviation s to provide a confidence level. The confidence level denotes the proportion of measurement values (percentage) inside the Gaussian distribution of the sensor's measurement findings, such as 68% for $\pm$ one standard deviation s (U68), or 95% for $\pm 2s$ (U95) (JCGM, 2008). U95 is utilized for the majority of engineering applications, as a tolerance of 5% outliers is permissible in most industrial contexts.

The total measurement value comprises the device's measured value and an associated uncertainty with a designated confidence level, specifically U95 in this instance. To assess the systematic deviation and uncertainty of pose measurements with a ChArUco calibration target, a calibration standard—a Faro measuring arm (Platinum 2.4m, Fig. 5)—is employed. The Faro arm has a U95 of 25 μm for point measurements and 36 μm for volumetric measurements (Faro, 2010), as ascertained by a methodology for evaluating measurement uncertainty in articulated arm coordinate measuring devices detailed in (Dain Johnson, 2019).

The measuring arm is calibrated prior to use, as outlined in the user handbook, and positioned between the ChArUco target and the camera system. The image acquisition was performed with a sCMOS camera pco panda DS26. The resolution was varied during the experiments by activating 2×2 binning, yielding a resolution of 2560×2560 or at full frame resolution of 5120×5120 pixels. Five Canon EF lenses with different focal lengths and apertures according to typical wind tunnel flow experiments were used. The active lens was positioned on a motorized tilt mount at a back focal length of 44 mm, which is standard for Canon EF lenses. The focus is adjusted using a remote focus ring that regulates both the focus and aperture of the lenses. The target is initially observed with a fully open aperture and subsequently adjusted to an f-stop of 5.6, which provides adequate depth of field for examining the inclined target plane, even at tilt angles of up to 70 ° around the target's y-axis.

A conventional ChArUco target comprising 15×24 markers, with a checker marker size of 20 mm and an ArUco marker size of 15 mm (DICT_5x5_1000, Fig. 1) was utilized, as well as a customized ChArUco board with 20×24 markers, with a checker marker size of 30 mm for larger working distances and ROI's (Fig. 6). The targets are affixed to a motorized turntable with a resolution of 0.01 ° and a repeatability of 0.001 °.
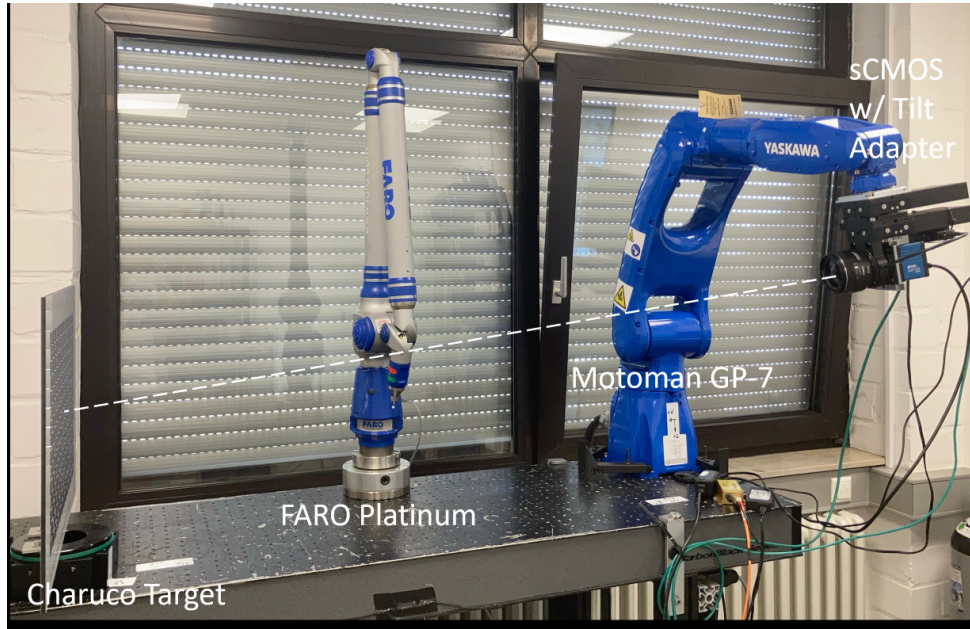

Figure 5: sCMOS camera mounted on GP-7 robot arm rotated around *x* and *y* axis, pointing towards the center of the ChArUco target plate. FARO measuring arm was used as position reference.

To facilitate rotation around the x and y axes of the target, the camera was affixed to a robotic arm (YASKAWA Motoman GP-7) and oriented towards the center of the target. This configuration is employed to validate the translational deviation along the x and y axes of the target. The positional repeatability of the GP-7 is ±10 μm in accordance with ISO 9283 standards. The robot controller facilitates
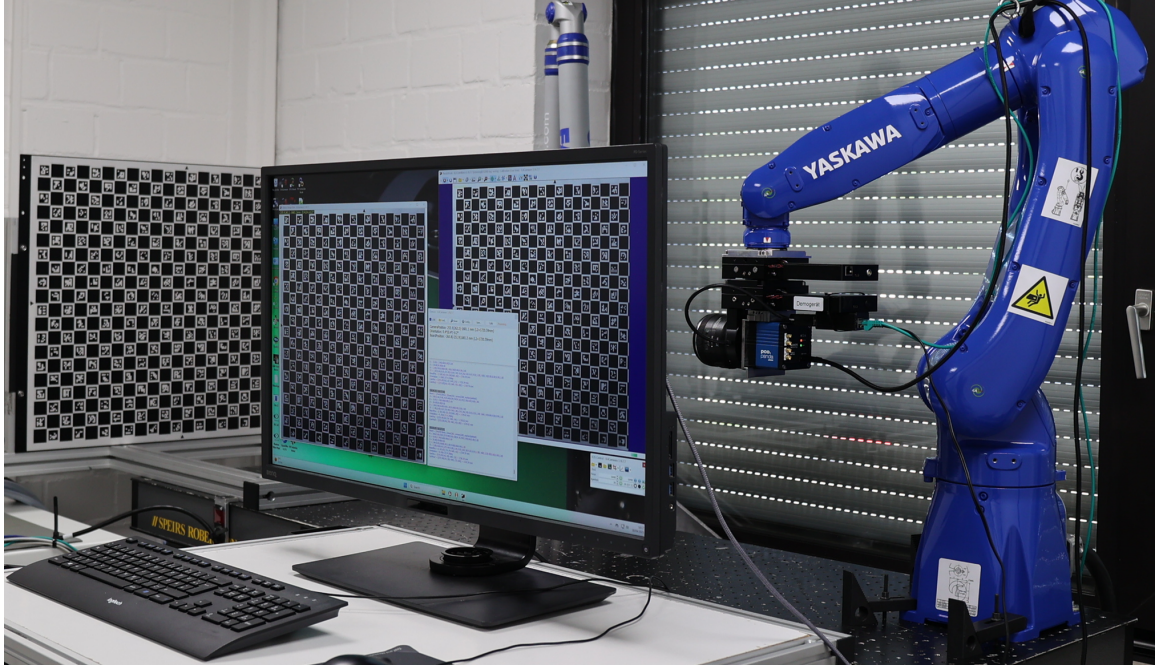
Figure 6: Complete calibration setup with a large customized ChArUco target and live image of the calibration process
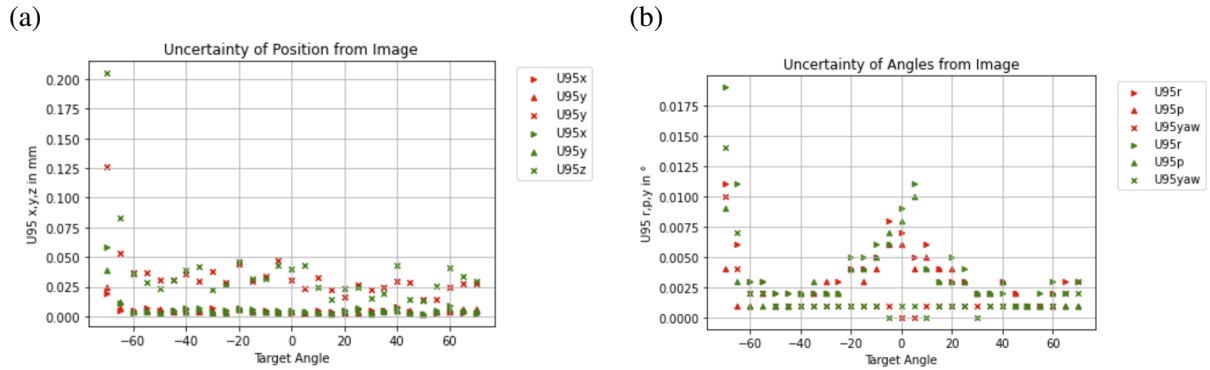
(a)

(b)

Figure 7: Uncertainty (repeatability) from single images (a) position, (b) angle.

rotation around the center of the ChArUco target through the utilization of 'user frames'.

The whole toolchain for identifying the target's posture is executed in the Robot Operating System (ROS) (Stanford Artificial Intelligence Laboratory et al., 2020) utilizing the charuco_detector package (Carlos da Costa, 2022), which produces a 6D pose of the target in camera coordinates. The measurements are produced utilizing two calibration files: one containing the theoretical values of the camera's intrinsic matrix (NoCalib) and the other comprising the intrinsic matrix derived by calibration with a standard 5×7 checkerboard with 25 mm squares (Calib). The theoretical parameters of the Non-Calib intrinsic matrix, specifically fx, fy, cx, and cy, are derived from the focal length of the employed Canon lens and the principal ray anchored to the geometric center of the sensor at coordinates (1280, 1280 in binned mode or 2560, 2560 in full resolution). The six-dimensional stance is derived from one hundred photos. The U95 of the pose estimation for a single image is computed for the x, y, and z coordinates, as well as the angles of roll r, pitch p, and yaw, as seen in Fig 1.

To assess the stability of the pose estimation using only a few markers within the field of view, the camera was translated parallel to the target. A minimum of four markers is required for valid detection, necessitating at least a 3×3 subgroup of the target. The camera was inclined by a roll angle of 15 °around the target's x-axis and thereafter tilted to angles of up to ±70°.

All poses (including inclination angles and positions) are referenced by the Faro arm, which acquires ten points on the target to establish the plane and the left bottom corner, serving as the origin of the ChArUco target seen in Fig 7. The coordinates for each point represent the mean of ten individual

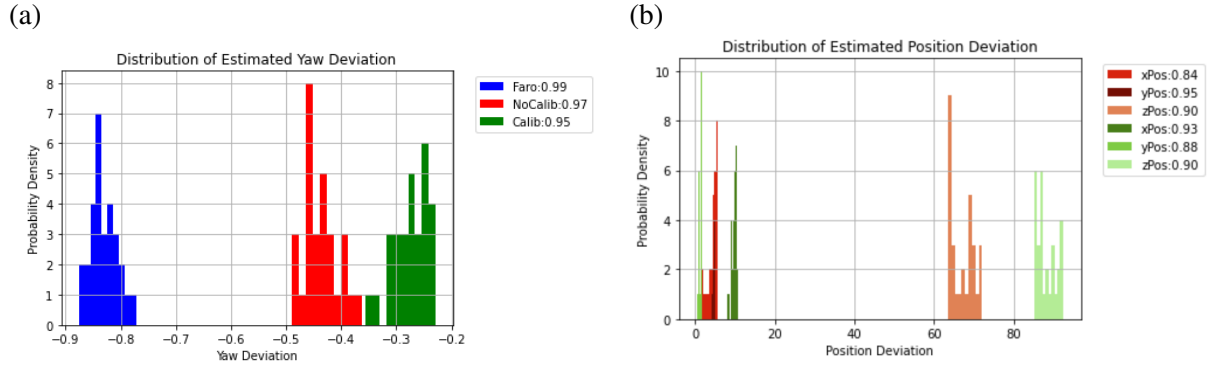(a)   (b)

Figure 8: Probability density of (a) yaw angle deviation, (b) position deviation.

measurements. The flatness of the collected planes was assessed and measured to be less than $100\,\mu m$ for the entire experiment. The camera's position is referenced by the Faro arm via a specialized tool affixed to the camera's front plane, indicating the sensor plane.

4   Results

The subsequent section presents the results about the overall measurement uncertainty of position detection with ChArUco targets for one specific lens configuration (EF335mm). Additionally, several camera lenses are evaluated based on positional accuracy for standard wind tunnel operating distances.

The measurement uncertainty U95, defined as twice the standard deviation, is applicable solely to a Gaussian distribution of the measurement data. A Shapiro-Wilk test from the SciPy.stats statistics package is employed to assess normality (The SciPy community, 2024). The probability density function of the predicted yaw angle and positional distribution is illustrated in (Fig 8), with the legend displaying the results of the Shapiro test. Values approaching 1.0 and exceeding 0.8 signify a Gaussian distribution. The subsequent measurement uncertainties can be computed under the assumption of a normal distribution of the data sets.

In comparing the results of the yaw angle estimation for the inclined ChArUco target, a greater deviation of the calibrated camera is evident (Fig. 9).

All three data sets yield somewhat reduced results for the yaw angle. The turntable served as a reference point. The following table is produced after computing the average values over all measured angles and incorporating the systematic errors:

System	Mean to Turn Table	U95 to Turn Table	Mean to Faro	U95 to Faro
not calibrated	-0.44°	0.06°	0.39°	0.07°
calibrated	-0.27°	0.06°	0.56°	0.06°
Faro arm	-0.83°	0.05°	NA	NA

The Faro data indicate a consistent systematic variation of approximately -0.8° relative to the turntable due to the absence of initial referencing to align the turntable and Faro angle. The calibrated camera exhibits a marginally reduced deviation from the turntable reference compared to the non-calibrated camera, however is positioned at a greater distance from the Faro (Fig. 9). The positional derivations can solely be linked to the Faro system, ensuring that all subsequent measurement data pertains to the Faro measuring arm.

The comparison of the target position divergence from the marker detection against the Faro data reference yields the following table, with all values expressed in [mm]:

System	D_x	$U95_{Dx}$	D_y	$U95_{Dy}$	D_z	$U95_{Dz}$
not calibrated	4.41	2.22	4.71	0.44	67.14	5.77
calibrated	9.71	1.40	1.32	0.63	88.27	4.79

The conclusion is evident: the calibrated camera yields a greater systematic deviation for both the x and z position estimates, but the y deviation is slightly lower. The uncertainties of both systems are

comparable; however, the deviation of the non-calibrated camera has a narrower range (Fig. 10). The discrepancy in the z location for both systems can be elucidated by the camera pinhole model employed for the 3D to 2D point transformation in imaging applications.

The camera coordinate frame's origin is situated at the center of the lens assembly, rather than at the center of the detector array. Consequently, the sensor distance z_{sd}, which denotes the location of the camera coordinate frame origin for reference with the measuring arm, can be determined by summing the back focal length b_{fl} with the focal length f of the employed lens:

$$z_{sd} = f + b_{fl} \tag{1}$$

The common value for Canon EF series is $b_{fl} = 44$ mm and $f = 35$ mm (for the EF 35mm), resulting in $z_{sd} = 79$ mm, which is close to the experimental value of approximately 67 mm. The Canon data sheet indicates a lens length of 62.5 mm, allowing for an estimation of the lens package center at approximately 31 mm from the mounting flange's end, which results in a sensor distance of $z_{sd} \approx 78$ mm.

Upon comparing position deviation as a function of the inclined yaw angle, it is evident that the calibrated camera exhibits a greater divergence from the reference than the non-calibrated data. Another observable impact is the dependence of the x position deviation on the inclination angle, but the y position is not significantly affected by the yaw angle.

Subsequent to confirming the approach using the described manner, supplementary measurements are conducted utilizing the configuration illustrated in Fig. 5 by repositioning the camera to various angles with an inclined ChArUco target. The coordinate frame for the robot was established near the center of the ChArUco target. The camera's position is consistently referred to the Faro measuring arm, as previously defined, and the origin of the ChArUco target remains at the specified place in Fig 1.

The camera is initially moved parallel to the target without any tilt in the x direction until less than four markers are visible, indicating that valid detection is no longer achievable. The deviation in the z position closely resembles that of the prior experiment, whereas the deviations in the x and y positions are less than those observed in the inclined experiments (Fig. 11).

In the inclined position estimation test, where roll (r) was held constant and pitch (p) was varied, non-calibrated camera data was utilized due to its reduced deviance relative to the calibrated system. The camera was directed at the target with a roll angle of $r = 15°$ around the x axis. With a pitch angle of $0°$ around the y-axis, the camera is initially positioned to capture the entire target, ensuring 100% sight of the markers. Subsequently, the target is rotated by 15, 25, 40, 50, and 70°. The camera is adjusted to ensure that only 75% of the markings are visible at a 0-°tilt (pitch) angle. This is reiterated for 50% and 25% visibility of the markers, with the pitch angle at 25% lowered to a maximum of $p = 55°$. At elevated angles, insufficient marks are discernible.

Figure 12 illustrates that the deviation in the x position remains consistent, even at elevated tilt angles of 50°, within the range of 5-6 mm, while the deviation in the y position is slightly lower. The computed angles indicate a roll deviation of approximately -0.5°, with tilt angles in the 50°-range and a similar pitch divergence of about +0.6°.

Finally, different lenses were analyzed to evaluate the attained accuracies. This assumption is significant, as an increased number of integrated lenses in the objectives amplifies deviations from the pinhole model. The significance of these variances was examined using lenses (EF standard) with focal lengths of 28 mm, 50 mm, 85 mm, and 100 mm. These lenses are generally utilized at object distances ranging from 1 to 3 meters. Fig. 13 illustrates the standard positions (z) calculated based on the ChArUco Target data in relation to the distances recorded with the FARO Arm. The camera location has been adjusted to align with the sensor position for direct comparison. The graph illustrates the anticipated trend, with
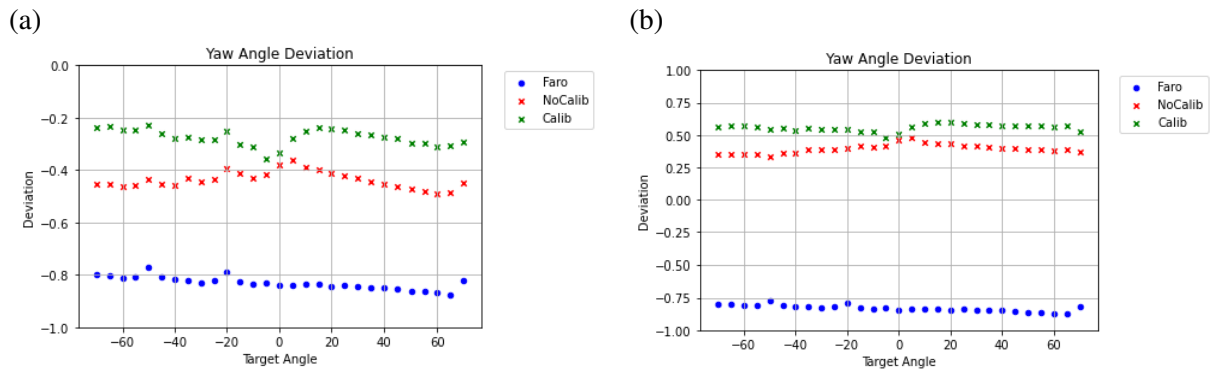
(a)

(b)

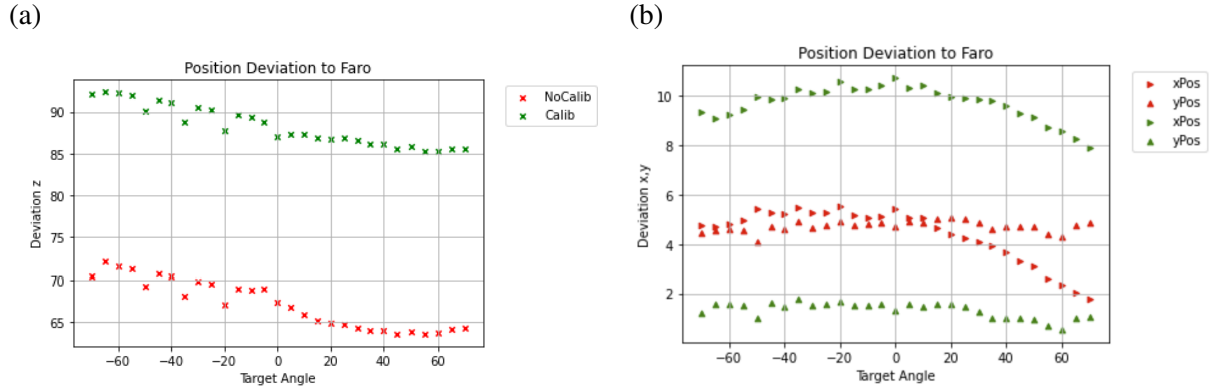Figure 9: Yaw angle deviation (a) referenced to turn table, (b) referenced to Faro arm.

(a)   (b)

Figure 10: Position deviation: green is Calib, red NoCalib (a) z position, (b) x, y position

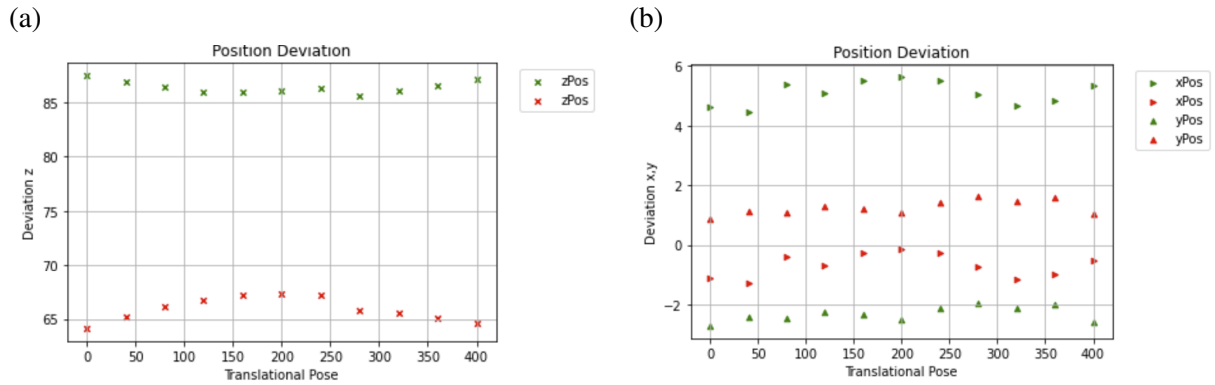(a)   (b)

Figure 11: Translational pose deviation: green is Calib, red NoCalib (a) z position, (b) x, y position

only slight variances observed at short focal lengths, or low magnifications. As focal lengths increase, these values rise but remain under 1.5% of the observed distances, validating the first given findings.

An overview of the averaged deviations [mm] between Faro arm measurement data and target marker detection within applied to the working distances shown in Fig. 13 is shown for the additional lenses tested. The calibration reduces the deviations significantly. However, if the lens system becomes more complex as it does for longer focal lengths the principal point cannot be estimated more accurately by using the pinhole model. Other model approaches have to be used instead.

Camera lens	EF 28 mm	EF 35 mm	EF 50 mm	EF 85 mm	EF 100 mm
D_z [mm] not calibrated	27.1	18.0	20.3	26.7	29.9
D_z [mm] calibrated	7.8	6.5	2.6	9.4	36.6

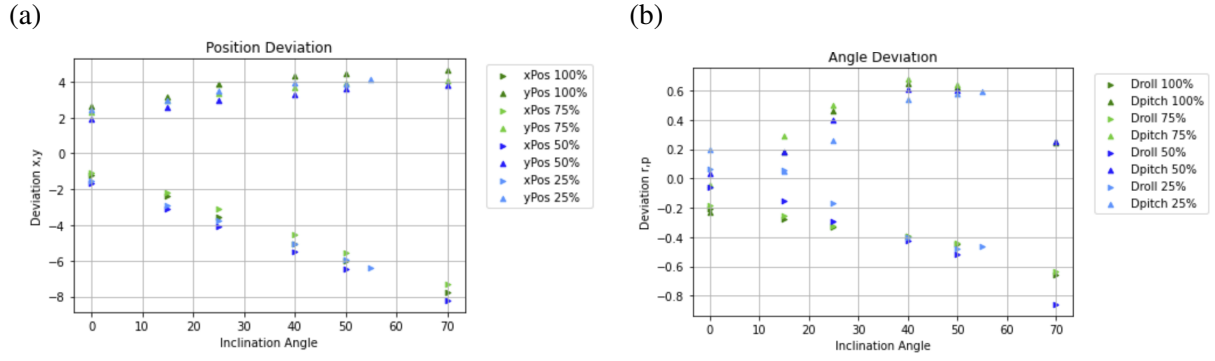(a)   (b)

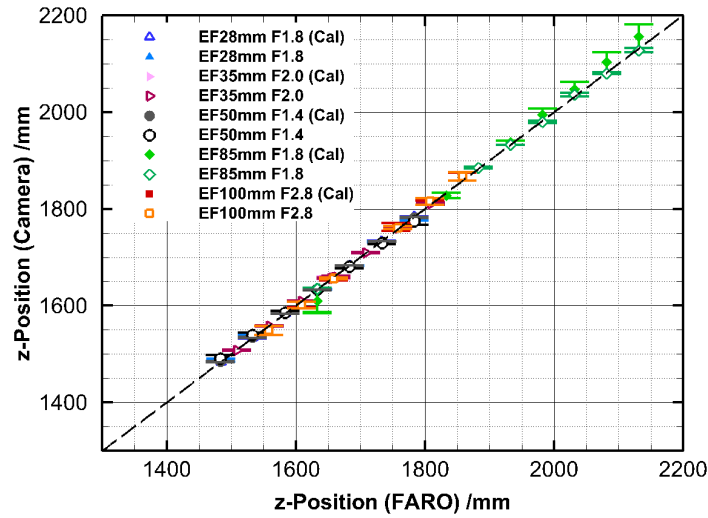Figure 12: Rotational Pose deviation (a) x, y position, (b) roll r, pitch p angles

Figure 13: Comparison of different Canon EF lenses: normal displacement (z) from Camera principle point to target origin, measured by FARO arm and data output of calibration

5 Conclusions

The utilization of fiducial markers can significantly streamline the configuration of a PIV system. The camera calibration method using standard checkerboards to obtain the intrinsic camera matrix can be omitted. Intrinsic parameters for a camera equipped with a nearly distortion-free SLR lens, along with specified pixel size and image sensor dimensions, can be obtained from the relevant data sheet. The camera coordinates may be accurately determined for most PIV systems with a working distance of approximately 2 m, given a measurement uncertainty of about 2.5 mm in the x-axis, 0.5 mm in the y-axis, and 6 mm in the z-axis. The estimation of the roll and tilt angle is exceptionally low, approximately 0.5°, for commonly used tilt angles below 50° and remains effective at elevated tilt angles near 70° for back-scatter PIV configurations. If the estimation deviates beyond a certain millimeter range, the camera can be incrementally adjusted to the target position by referencing the initial estimation of the camera pose and making the necessary corrections, even in cases when the markers are not fully visible.

It has been determined that fewer than 50% of the board markers are enough for the reliable detection of the calibration grid at tilt angles of up to 70° (Fig. 14).

An assessment of the uncertainty at extended working distances can be conducted by utilizing a laser tracker as a reference point. However, the camera must be calibrated, for instance, for the de-warping process in stereo PIV, after positioning by creating a mapping function with the requisite point correspondences. However, the implementation of a calibration target featuring fiducial markers facilitates comprehensive automatic calibration (Fig. 15) by identifying the marker IDs and their respective corners to establish the correspondence between real-world and pixel coordinates through the back-projection of the known corner positions.

In the final phase of calibration, a disparity correction utilizing recorded particle pictures addresses the remaining misalignment between the laser light sheet and the calibration target.
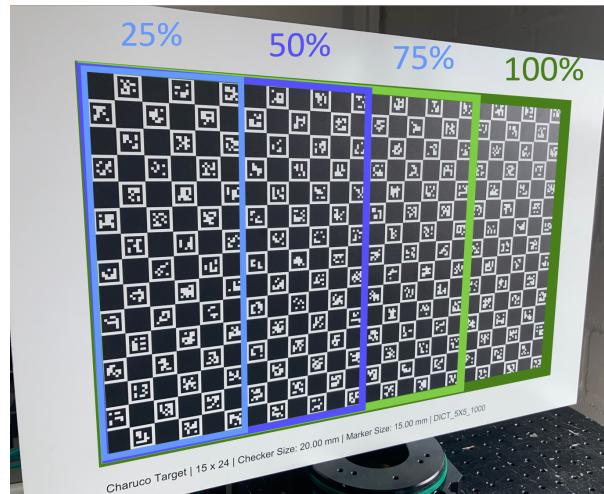
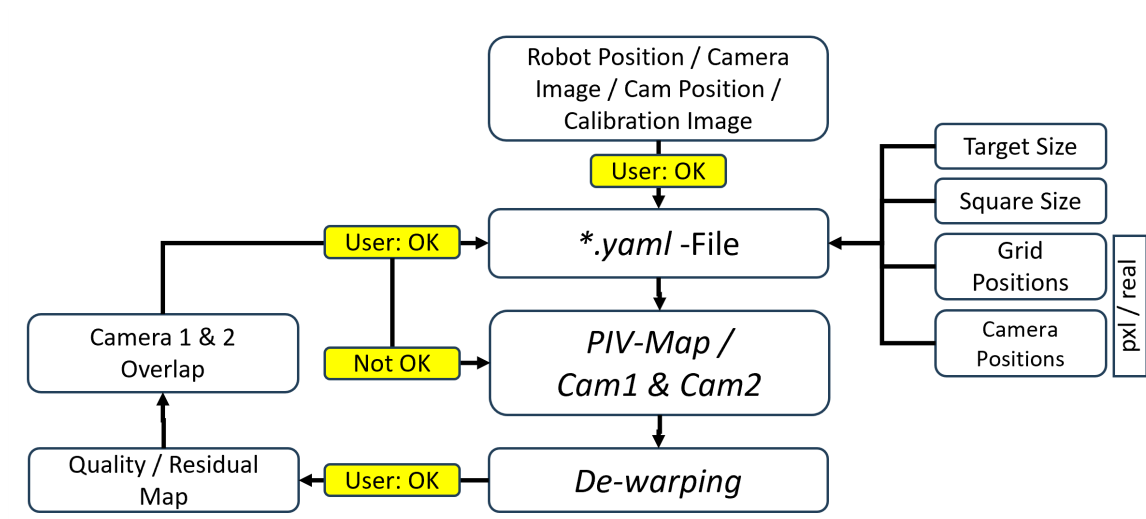Figure 14: Illustration of visible/used markers for valid calibration data

Figure 15: Workflow of calibration within the software environment of *PIVView 4.0*

References

Akamine M, Teramoto S, and Okamoto K (2023). Formulation and demonstrations of three-dimensional background-oriented schlieren using a mirror for near-wall density measurements. *Exp. Fluids* 64(134). doi:10.1007/s00348-023-03672-1. URL https://doi.org/10.1007/s00348-023-03672-1

Carlos da Costa (2022). charuco_detector. URL https://github.com/carlosmccosta/charuco_detector

Dain Johnson (2019). Calibration of articulating arm coordinate measuringmachines per asme b89.4.22-2004. In *19th International Congress of Metrology, 09005 (2019)*. doi:https://doi.org/10.1051/metrology/201909005

DIN (1995). Grundlagen der Messtechnik - Teil 1: Grundbegriffe

Faro (2010). Faroarm platinum, main documentation, version: 2.4m. URL https://www.faro.com/measuring-arms

Garrido-Jurado S, Muñoz-Salinas R, Madrid-Cuevas F, and Marín-Jiménez M (2014). Automatic generation and detection of highly reliable fiducial markers under occlusion. *Pattern Recognition* 47(6):2280–2292. ISSN 0031-3203. doi:10.1016/j.patcog.2014.01.005. URL https://www.sciencedirect.com/science/article/pii/S0031320314000235

JCGM (2008). Evaluation of measurement data — Guide to the expression of uncertainty in measurement. doi:10.59161/JCGM100-2008E. URL `https://doi.org/10.59161/JCGM100-2008E`

Krogius M, Haggenmiller A, and Olson E (2019). Flexible layouts for fiducial tags. In *2019 IEEE/RSJ International Conference on Intelligent Robots and Systems (IROS)*, p. 1898–1903. IEEE Press. doi:10.1109/IROS40897.2019.8967787. URL `https://doi.org/10.1109/IROS40897.2019.8967787`

Olson E (2011). AprilTag: A robust and flexible visual fiducial system. In *2011 IEEE International Conference on Robotics and Automation*, pp. 3400–3407. doi:10.1109/ICRA.2011.5979561

Stanford Artificial Intelligence Laboratory et al (2020). Robotic operating system. URL `https://www.ros.org`

The SciPy community (2024). scipy.stats.shapiro. URL `https://docs.scipy.org/doc/scipy/reference/generated/scipy.stats.shapiro.html`

Zakiev A, Tsoy T, Shabalina K, Magid E, and Saha S K (2020). Virtual experiments on ArUco and AprilTag systems comparison for fiducial marker rotation resistance under noisy sensory data. In *2020 International Joint Conference on Neural Networks (IJCNN)*, pp. 1–6. doi:10.1109/IJCNN48605.2020.9207701